Superhydrophilic NiFe-LDH@Co$_9$S$_8$-Ni$_3$S$_2$/NF heterostructures for high-current-density freshwater/seawater oxidation electrocatalysts

Liying Liu [a], Yangyang Chen [a], Qi Zhang [a], Zhe Liu [a], Kefen Yue [a,*], Yongliang Cheng [a,*], Dongsheng Li [b], Zhonghua Zhu [c], Jiayao Li [a], Yaoyu Wang [a]

[a] *Key Laboratory of Synthetic and Natural Functional Molecule of the Ministry of Education, Xi'an Key Laboratory of Functional Supramolecular Structure and Materials, College of Chemistry and Materials Science, Northwest University, Xi'an 710127, China*
[b] *College of Materials and Chemical Engineering, Key Laboratory of Inorganic Nonmetallic Crystalline and Energy Conversion Materials, China Three Gorges University, Yichang 443002, China*
[c] *School of Chemical Engineering, the University of Queensland, Brisbane 4072, Australia*

ARTICLE INFO

ABSTRACT

Designing oxygen evolution reaction (OER) electrocatalysts with high efficiency and stability at large current densities is paramount for achieving hydrogen production through water splitting. In this study, a heterostructured NiFe-LDH coating Co$_9$S$_8$-Ni$_3$S$_2$ grown on nickel foam (NiFe-LDH@Co$_9$S$_8$-Ni$_3$S$_2$/NF) was successfully synthesized. The distinctive hierarchical structures featuring abundant heterointerfaces can effectively expose abundant active sites. The synergistic effect and strong electronic interaction between Co$_9$S$_8$-Ni$_3$S$_2$ and NiFe-LDH can enhance the intrinsic OER activity. Furthermore, the superhydrophilic characteristic of NiFe-LDH@Co$_9$S$_8$-Ni$_3$S$_2$/NF favors close contact between the electrode and electrolyte. Due to these advantages, NiFe-LDH@Co$_9$S$_8$-Ni$_3$S$_2$/NF can provide distinguished OER activity with low overpotentials of 274 mV in alkaline freshwater and 298 mV in alkaline seawater at 1000 mA cm^{-2}, along with outstanding stability at high current density of 500 mA cm^{-2} over 200 h in both solutions. This study offers a valuable insight into fabricating high-performance OER electrocatalysts for seawater electrolysis in industrial applications.

1. Introduction

Due to escalating concerns regarding energy and the environment, there is an immediate need to prioritize the advancement of renewable and eco-friendly energy sources and the conversion of CO$_2$ into valuable chemicals [1–4]. Nowadays, hydrogen is gaining attention as a pollutant-free substance and sustainable energy carrier that holds promise for reducing the use of chemical fuels and thereby mitigating environmental pollution [5,6]. At present, hydrogen production through electrocatalytic water splitting is attracting significant interest because of its mature technology, operational simplicity, and free of pollution [7–9]. The electrocatalytic water splitting consists of the hydrogen evolution reaction (HER) and the oxygen evolution reaction (OER) [10, 11]. Compared to HER, the OER with a four-step electron transfer process, possesses sluggish kinetics [12,13], thereby significantly limiting the effectiveness of water splitting. IrO$_2$ and RuO$_2$ are popular choices for high-efficiency OER electrocatalysts due to their precious metal nature [14,15]. Nonetheless, their high price and limited availability have

hindered their widespread application [16,17]. Therefore, there is an immediate requirement to exploit inexpensive yet effective and long-lasting OER electrocatalysts for OER.

Recently, transition metal sulfides have gained widespread attention as prospective OER electrocatalysts owing to their exceptional conductivity and capacity to exhibit diverse metal oxidation states [18]. Therefore, numerous researchers have been drawn to the fabrication of varieties of transition metal sulfides [19–21]. Despite significant advancements, the application of transition metal sulfides still encounters substantial challenges that need to be addressed. Firstly, the reported sulfides usually possess outstanding activity at relatively small current densities (smaller than 100 mA cm^{-2}) [22], but fall short of meeting the requirements for industrial-scale electrocatalytic water splitting. Secondly, the performances of the mostly reported sulfides were evaluated in an alkaline solution prepared using freshwater, which accounts for less than 4 % of the world's total water resources [23,24]. Consequently, the scarcity of freshwater would impose restrictions on industrial-scale electrocatalytic water splitting. In terms of this, direct seawater

---

electrocatalysis has emerged as an attractive strategy for hydrogen production, but its application is significantly hindered by the competition from chlorine evolution reactions (ClER) and corrosion caused by high concentrations of Cl⁻ [25,26]. Thirdly, sulfides usually present limited durability at large current densities [22]. Moreover, a significant amount of gas is generated under these conditions. The produced gas bubbles would adhere to the surface electrocatalyst, thereby obstructing active sites and impeding electrolyte diffusion, resulting in an increased overpotential [27]. Additionally, this elevated overpotential can accelerate ClER, thereby severely constraining the efficiency of direct seawater electrolysis [24,28].

Inspired by the factors mentioned above, herein we present a rational design and synthesis for a high current density OER electrocatalyst in alkaline freshwater and alkaline seawater. This electrocatalyst is composed of NiFe-LDH nanosheets with amorphous structure wrapped around Co_9S_8-Ni_3S_2 nanorods grown on nickel foam (NiFe-LDH@Co_9S_8-Ni_3S_2/NF) by hydrothermal method and subsequent electrodeposition. The obtained NiFe-LDH@Co_9S_8-Ni_3S_2/NF features amorphous-crystalline and triphasic interfaces, which can afford abundant active sites as well as enhance intrinsic activity. Additionally, the open structure and superhydrophilic characteristics can facilitate mass transfer efficiency. As a result, NiFe-LDH@Co_9S_8-Ni_3S_2/NF exhibits superior OER performance at high current densities in both alkaline freshwater and alkaline seawater environments. It demonstrates low overpotentials of 274 mV and 298 mV at 1000 mA cm^{-2} under conditions of alkaline freshwater and alkaline seawater, respectively, along with outstanding stability for over 200 hours at 500 mA cm^{-2}. The present study provides a feasible approach and valuable insights into the fabrication of high-performance electrocatalysts for efficient seawater electrolysis in industrial applications.

2. Experimental section

2.1. Chemicals

Ferrous sulfate heptahydrate ($FeSO_4 \cdot 7\ H_2O$, 99 %), Nickel nitrate hexahydrate ($Ni(NO_3)_2 \cdot 6\ H_2O$, 99 %), urea (99 %), ammonium fluoride (96 %), Cobalt nitrate hexahydrate ($Co(NO_3)_2 \cdot 6\ H_2O$, 99 %), Sodium sulfide nonahydrate ($Na_2S \cdot 9\ H_2O$, 99 %), and commercial IrO_2 (99 %). All chemicals (analytical grade) were bought from commercial sources and without further purification treatment.

2.2. Pretreatment of NF

The NF (1×3 cm^2) substrate underwent a series of cleaning steps, including ultrasonic washing in anhydrous ethanol, deionized water, 2 M hydrochloric acid, deionized water, and anhydrous ethanol, each for a duration of 10 min. Subsequently, it was vacuum dried at 60 ℃ for 8 h. Untreated NF was bought from commercial sources.

2.3. Preparation of Ni-Co precursor/NF

A total of 1 mmol of nickel source and cobalt source (1:2), along with 5 mmol of urea and 2 mmol of NH_4F, were added to 16 mL of deionized water. After stirring to dissolve, the mixture was diverted into a 25 mL autoclave. Following that, the pre-treated NF was introduced into the mixture. The autoclave was subsequently subjected to heating at 120 ℃ for 10 h. Following this, the resulting Ni-Co precursor/NF underwent several rounds of washing using distilled water and anhydrous ethanol before being subjected to vacuum drying.

2.4. Preparation of Co_9S_8-Ni_3S_2/NF

The initial step involved dissolving $Na_2S \cdot 9\ H_2O$ (1 mmol) in deionized water (18 mL), followed by transferring the solution to a 25 mL autoclave. Subsequently, the Ni-Co precursor/NF was introduced into

the solution. The autoclave was then heated in an oven for 12 h at 120 ℃. The resulting Co_9S_8-Ni_3S_2/NF underwent consistent cleaning and drying procedures, as previously described.

2.5. Preparation of NiFe-LDH@Co_9S_8-Ni_3S_2/NF

Throughout the entire electroplating process, a mixed solution of Ni(NO_3)$_2$ and $FeSO_4$ (1:1) with a total concentration of 0.1 M was used as the electrolyte. The potential and time were set at -1.1 V and 500 s, respectively. Following a similar procedure, NiFe-LDH/NF was synthesized by replacing Co_9S_8-Ni_3S_2/NF with NF. Both NiFe-LDH@Co_9S_8-Ni_3S_2/NF and NiFe-LDH/NF underwent cleaning and drying using the previously mentioned consistent steps.

2.6. Preparation of IrO_2/NF and Pt/C/NF

Firstly, 4 mg of IrO_2 powder was added to the mixed solution composed of 20 μL of Nafion and 480 μL of isopropanol. The mixture was then subjected to ultrasonic treatment. Subsequently, 400 μL of the resulting mixture was dropped onto a clean NF (1×1 cm^2) and dried using an infrared lamp to obtain the IrO_2/NF electrode. The preparation process for the Pt/C/NF electrode followed the same steps as described above, with the substitution of IrO_2 powder with Pt/C powder.

2.7. Characterization

The Bruker D8 X-ray diffraction (XRD) instrument was used for analyzing the composition of the material. A Raman spectrometer (LabRAM HR Evolution) was utilized to gain the sample Raman spectra. Infrared spectroscopy testing was conducted using the Bruker Tensor-27 FT-IR spectrometer. The Hitachi SU8010 scanning electron microscope (SEM) was utilized to acquire the surface appearance of the materials. The FEI Talos F200X transmission electron microscope was used for performing high-resolution TEM (HRTEM) imaging, and the elements were analyzed using Energy-Dispersive X-ray (EDX) spectroscopy. The ULVAC-PHI5000 VersaProbeIII instrument with X-ray photoelectron spectroscopy (XPS) measured the chemical properties of the material. The hydrophilicity of the prepared material was investigated by the Contact Angle measuring instrument (OCA25). Inductively Coupled Plasma Mass Spectrometry (ICP-MS, Agilent 7900) was employed to analyze the content of Ni, Co, Fe and S in the electrolyte.

2.8. Electrochemical measurements

The OER performance was investigated using the CHI 660E and CS 350 electrochemical workstations. Hg/HgO and carbon rod were employed as reference electrode and counter electrode, respectively. All values were standardized to reversible hydrogen electrodes using the equation of

$$E_{RHE} = E_{Hg/HgO} + 0.098 + 0.059 \times pH$$

The linear sweep voltammetry (LSV) curves were obtained at a scan rate of 5 mV s^{-1}. The electrochemical double-layer capacitance (C_{dl}) was determined by conducting cyclic voltammetry (CV) experiments at various scan rates (20–60 mV s^{-1}) within the non-Faraday region (0.95–1.05 V vs. RHE). Electrochemical impedance spectroscopy (EIS) was performed over the frequency range of 100 kHz to 0.1 Hz. The Faraday efficiency was evaluated through the water drainage method, while the volume of theoretically produced O_2 was calculated by the following equation:

$$V = i \times t \times 22.4/(n \times F)$$

where V represents the volume of O_2 (L), F represents Faraday's constant in units of C mol^{-1}, i represents the applied current in amperes (A), n represents the number of moles of electrons transferred required to

produce 1 mol O_2, and t represents the duration of the test in seconds (s).

All experiments were conducted at room temperature, and iR compensation was implemented for all measured curves except the marked data.

3. Results and discussion

3.1. Compositional and structural characterization of electrocatalysts

The specific synthesis procedure for NiFe-LDH@Co_9S_8-Ni_3S_2/NF is illustrated in Fig. 1. The Ni-Co precursors were first fabricated on a NF using the hydrothermal method and then converted into Co_9S_8-Ni_3S_2/NF nanorod arrays through hydrothermal sulfidation. Finally, the hierarchically structured NiFe-LDH@Co_9S_8-Ni_3S_2/NF was fabricated through the electrodeposition of NiFe-LDH. The color of the samples changes from pink-purple to black and yellow-green during the synthesis process (Fig. S1). The loading is determined by comparing the weight of samples at different synthesis states, resulting in values of 4.67, 5.27 and 8.94 mg cm^{-2} for each state, respectively.

The crystalline structure of the samples at different stages was analyzed by XRD. The distinct peaks located at 44.5°, 51.8°, and 76.4° in the XRD pattern of Ni-Co precursor/NF are in line with the characteristic peaks of NF (JCPDS No. 04–0850). No characteristic peaks corresponding to Ni-Co precursors are observed, likely due to their weak diffraction peak intensity (Fig. 2a). To eliminate the influence of NF, the Ni-Co precursor was peeled from NF and then subjected to XRD characterization. The resulting diffraction peaks exhibit good alignment with the characteristic peaks of $Co(CO_3)_{0.5}OH$ (JCPDS No. 48–0083) (Fig. S2). After sulfidation, in addition to the diffraction peaks originating from NF (Fig. 2b), the peaks at 21.7°, 31.1°, 37.8°, 38.3°, 49.7°, 50.1°, 54.6°, and 55.2° belong to the (101), (110), (003), (021), (113), (211), (104), and (122) crystallographic planes of Ni_3S_2 (JCPDS No. 44–1418), respectively. While the presence of additional peaks at 17.9°, 29.8°, 39.5°, 40.6°, and 52.1° can be attributed to the (200), (311), (331), (420), and (440) crystallographic planes of Co_9S_8 (JCPDS No. 86–2273), respectively, these findings provide evidence of the accomplished transformation of Ni-Co precursor/NF into Co_9S_8-Ni_3S_2/NF. After the electrodeposition process (Fig. 2b), no notable peaks associated with NiFe-LDH are observed in the XRD pattern. Then Raman spectra were employed to confirm the composition (Fig. 2c), the identified peaks at 457 cm^{-1} and 542 cm^{-1} agree well with the disordered Ni^{II}-O, while the distinctive peak at 294 cm^{-1} originates from Fe^{III}-O species [29,30]. Furthermore, the peak at 375 cm^{-1} stems from the sulfides [31]. The above results confirm that NiFe-LDH with a disordered structure is successfully complexed with Co_9S_8-Ni_3S_2/NF to form heterostructured NiFe-LDH@Co_9S_8-Ni_3S_2/NF.

To investigate the functional groups presented in the samples, FT-IR spectroscopy was employed. As illustrated in Fig. S3, the presence of a prominent peak at 3425 cm^{-1} is connected with the OH$^-$ stretching vibration in water molecules [30]; the peak centered at 1384 cm^{-1} indicates the presence of NO_3^-; and the presence of the peak at 1631 cm^{-1} suggests the interlayer water molecules' bending vibration. The observed peaks at 673 and 619 cm^{-1} are likely a result of absorptions related to M-O bonds [32,33]. Additionally, the peaks at 1114 cm^{-1} belong to SO_4^{2-} anions [34]. This observation further validates the fabrication of NiFe-LDH on Co_9S_8-Ni_3S_2/NF.

The morphological evolution of the samples was analyzed through SEM. The primal NF displays a porous network structure with a smooth surface (Fig. S4). After undergoing hydrothermal treatment, Ni-Co precursor with interwoven nanowire structures were observed to grow on the surface of NF (Fig. 2d and g). Subsequent hydrothermal sulfidation led to a morphological transformation from nanowires to nanorods (Fig. 2e and h). After undergoing further electrodeposition, a layer of NiFe-LDH nanosheets is coated onto Co_9S_8-Ni_3S_2/NF, resulting in the formation of heterostructured NiFe-LDH@Co_9S_8-Ni_3S_2/NF (Fig. 2f and i). The establishment of this hierarchical heterostructure can provide accessible pathways and sufficient space to promote electrolyte penetration and gas release, thereby promoting OER activity at high current density [35].

The microstructural information of NiFe-LDH@Co_9S_8-Ni_3S_2/NF was further investigated through TEM analysis. A representative TEM image clearly demonstrates the wrapping of nanosheets on the surface of nanorods, forming a heterogeneous structure (Fig. 3a). The HRTEM image reveals two distinct lattice spacing measuring 0.225 and 0.300 nm (Fig. 3b), which align closely with the (420) planes of Co_9S_8 and the (122) plane of Ni_3S_2, respectively. No apparent lattice fringe is observed in the nanosheet region, suggesting that the structure of NiFe-LDH appears to be amorphous. Additionally, there is a distinct interface between Co_9S_8-Ni_3S_2 and NiFe-LDH, with close contact between the two phases, further confirming the establishment of heterostructure. Moreover, the EDX images display that the Ni, Fe, and O are homogenously distributed on the entire sample (Fig. 3c), while the Co and S elements are predominantly concentrated in the interior region of the sample, providing additional evidence for the formation of heterostructure.

The changes in electronic structure induced by the formation of heterostructure were investigated through the XPS technique. The presence of Ni, Fe, Co, S, and O elements is confirmed by the XPS survey spectrum of NiFe-LDH@Co_9S_8-Ni_3S_2/NF (Fig. 4a). For the Co 2p spectra of NiFe-LDH@Co_9S_8-Ni_3S_2/NF (Fig. 4b) [36], two distinct peaks were observed at energy levels of approximately 781.43 eV and around
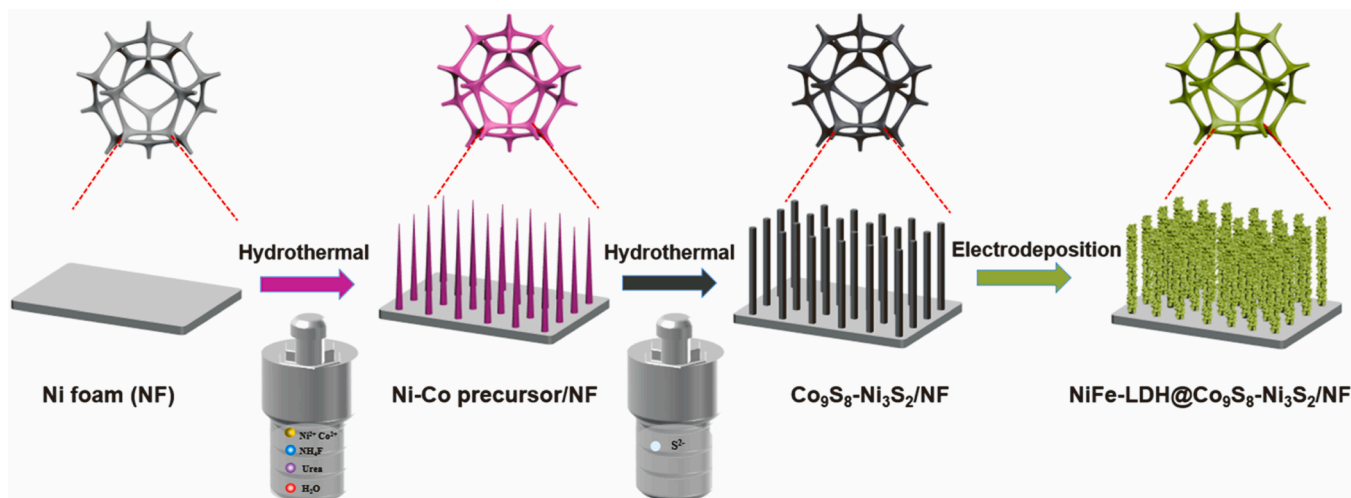

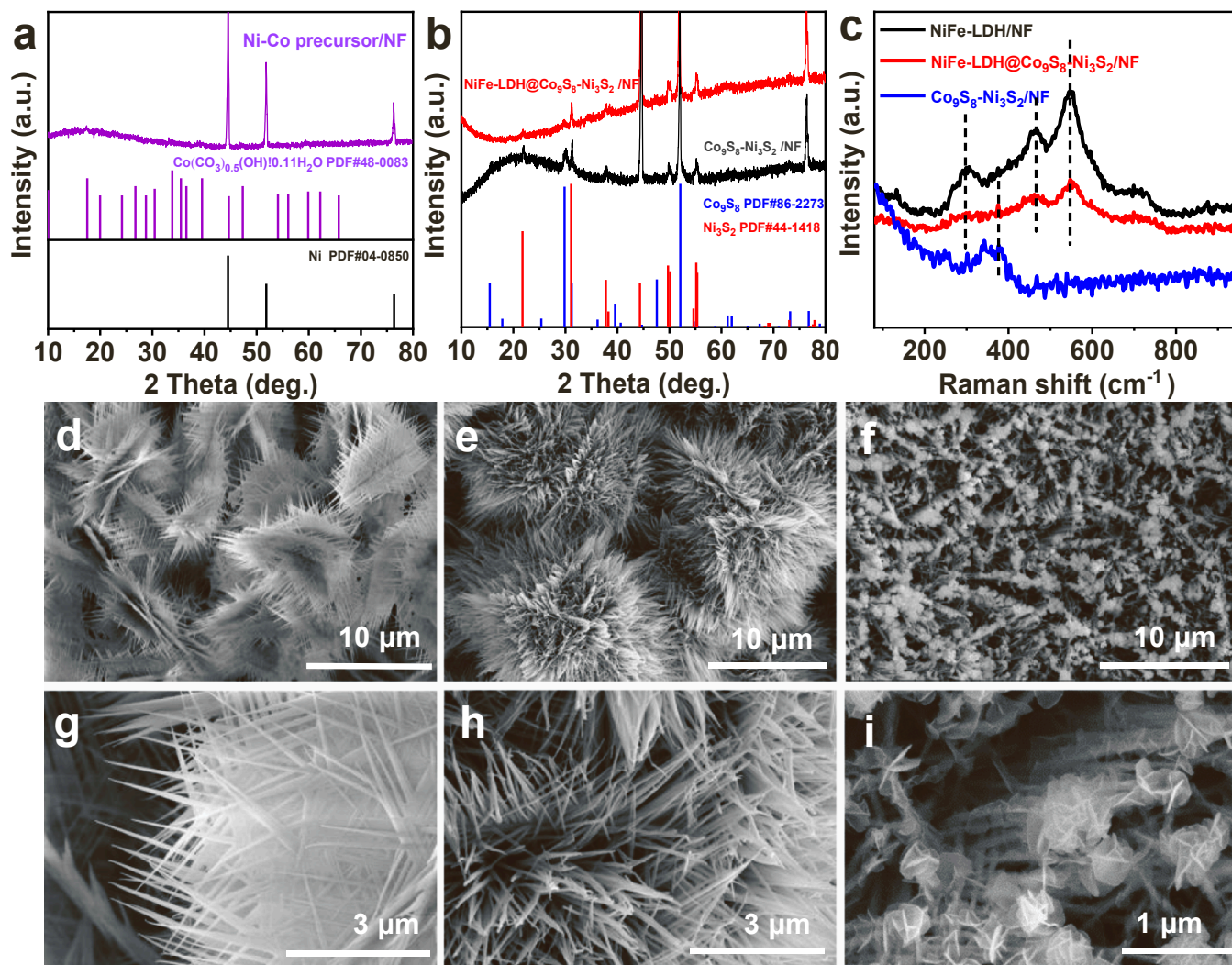**Fig. 1.** Schematic illustration of the synthesis procedure for NiFe-LDH@Co_9S_8-Ni_3S_2/NF.

Fig. 2. (a) XRD pattern of Ni-Co precursor/NF, (b) XRD patterns of Co_9S_8-Ni_3S_2/NF, and NiFe-LDH@Co_9S_8-Ni_3S_2/NF, (c) Raman spectra of NiFe-LDH/NF, NiFe-LDH@Co_9S_8-Ni_3S_2/NF and Co_9S_8-Ni_3S_2/NF, SEM images of (d, g) Ni-Co precursor/NF, (e, h) Co_9S_8-Ni_3S_2/NF and (f, i) NiFe-LDH@Co_9S_8-Ni_3S_2/NF.

796.80 eV, corresponding to Co $2p_{3/2}$ and Co $2p_{1/2}$, respectively. The fitted peaks observed at 780.30 and 795.40 eV are indicative of Co^{3+} species, while the peaks at 781.90 and 796.80 eV can be associated with the existence of Co^{2+} species. The additional peaks presented at 786.50 and 801.9 eV correspond to the satellite (labeled "Sat") peak [35]. In comparison with the Co_9S_8-Ni_3S_2/NF [37], a positive shift of 0.63 and 0.44 eV for Co $2p_{3/2}$ and Co $2p_{1/2}$ peaks are observed. The Ni 2p spectra of NiFe-LDH@Co_9S_8-Ni_3S_2/NF can be fitted into four peaks, which correspond to Ni $2p_{3/2}$, (855.69 eV), Ni $2p_{1/2}$ (873.28 eV), and two satellite peaks (Fig. 4c). The fitted binding energies of Ni $2p_{3/2}$ and Ni $2p_{1/2}$ suggest a +2 oxidation state for Ni in NiFe-LDH@Co_9S_8-Ni_3S_2/NF [38]. The binding energies of Ni $2p_{3/2}$ and Ni $2p_{1/2}$ in NiFe-LDH@-Co_9S_8-Ni_3S_2/NF are higher than those in Co_9S_8-Ni_3S_2/NF (855.62/873.22 eV) and smaller than those in NiFe-LDH/NF (855.93/873.81 eV) [39]. The above results indicate a robust electronic interaction between Co_9S_8-Ni_3S_2 and NiFe-LDH. The Fe 2p spectra of NiFe-LDH@Co_9S_8-Ni_3S_2/NF shows two peaks at 711.46 eV (Fe $2p_{3/2}$) and 724.85 eV (Fe $2p_{1/2}$) (Fig. 4d) [38]. These peaks demonstrate a negative shift in comparison to NiFe-LDH [40], reconfirming the presence of interaction between Co_9S_8-Ni_3S_2 and NiFe-LDH [41]. The S 2p spectra (Fig. 4e) of NiFe-LDH@Co_9S_8-Ni_3S_2/NF displays peaks at 163.6 and 162.2 eV, associated with S^{2-}, along with a peak at 168.66 eV, originating from SO_4^{2-}, which is positively shifted by 0.4 eV as compared

with that of Co_9S_8-Ni_3S_2/NF. The positive shifts of Ni 2p and S 2p demonstrated that the electron structure of Co_9S_8-Ni_3S_2 was successfully modulated due to the establishment of heterostructures with NiFe-LDH. The weakening intensity of the S^{2-} peak was attributed to both the formation of heterostructure and the limited detection depth of XPS technology [42]. Besides, the strong intensity of the peak corresponding to SO_4^{2-} can be attributed to intercalated SO_4^{2-} during the synthesis process [43]. The O 1 s spectra of NiFe-LDH@Co_9S_8-Ni_3S_2/NF exhibits three distinct fitted peaks (Fig. 4f), representing the metal-oxygen bond, hydroxides, and adsorbed H_2O, respectively [41,44].

The performance of the electrocatalyst is greatly impacted by its hydrophilicity, particularly at high current density, which is affected by its microstructure. The stronger the hydrophilicity, the faster the mass transfer rate, thereby facilitating the adsorption of water molecules during the reaction [45]. Besides, the enhancement of hydrophilicity will result in a more pronounced aerophobic performance, which can facilitate the rapid elimination of gas bubbles. For bare NF, its contact angle is 93.56° (Fig. 5a), indicating its poor hydrophilicity. However, upon the establishment of NiFe-LDH@Co_9S_8-Ni_3S_2 on NF, the contact angle decreases to 0° (Fig. 5b), revealing its excellent hydrophilicity. Moreover, as demonstrated in Movie S1, a water droplet is instantaneously absorbed upon contacting the surface of NiFe-LDH@Co_9S_8--Ni_3S_2/NF, further substantiating its strong hydrophilicity.
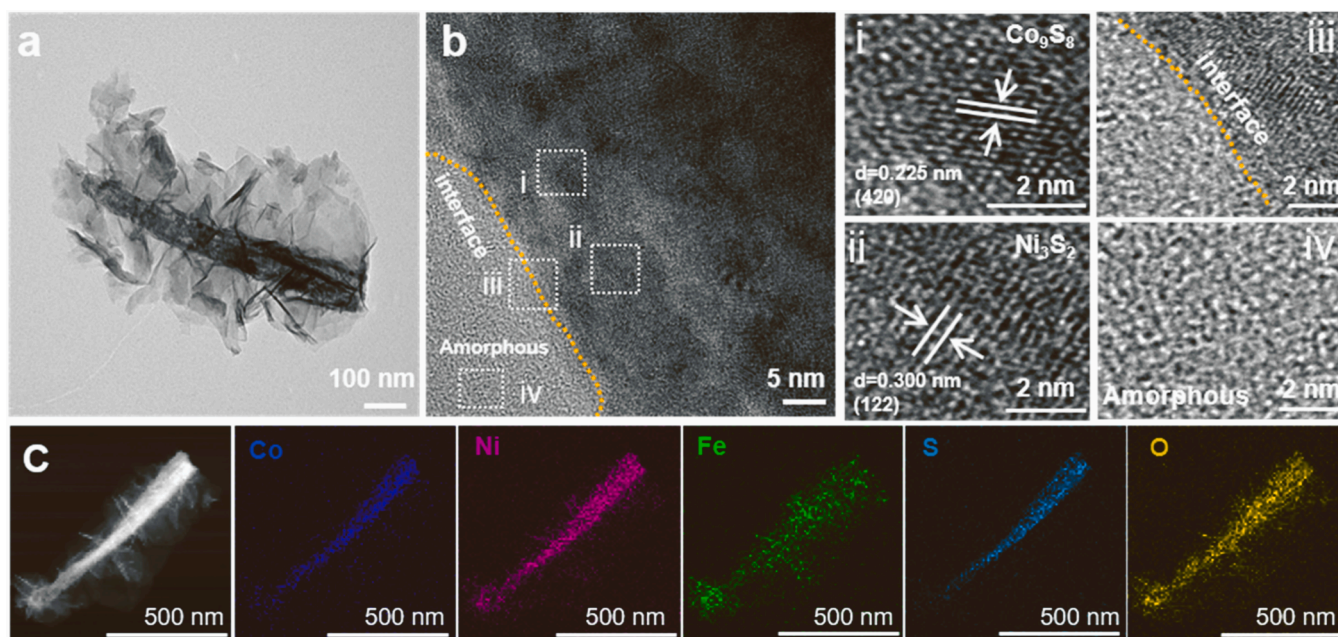
Fig. 3. (a) TEM image, (b) HRTEM image and (c) EDX elemental mapping of NiFe-LDH@Co₉S₈-Ni₃S₂/NF.
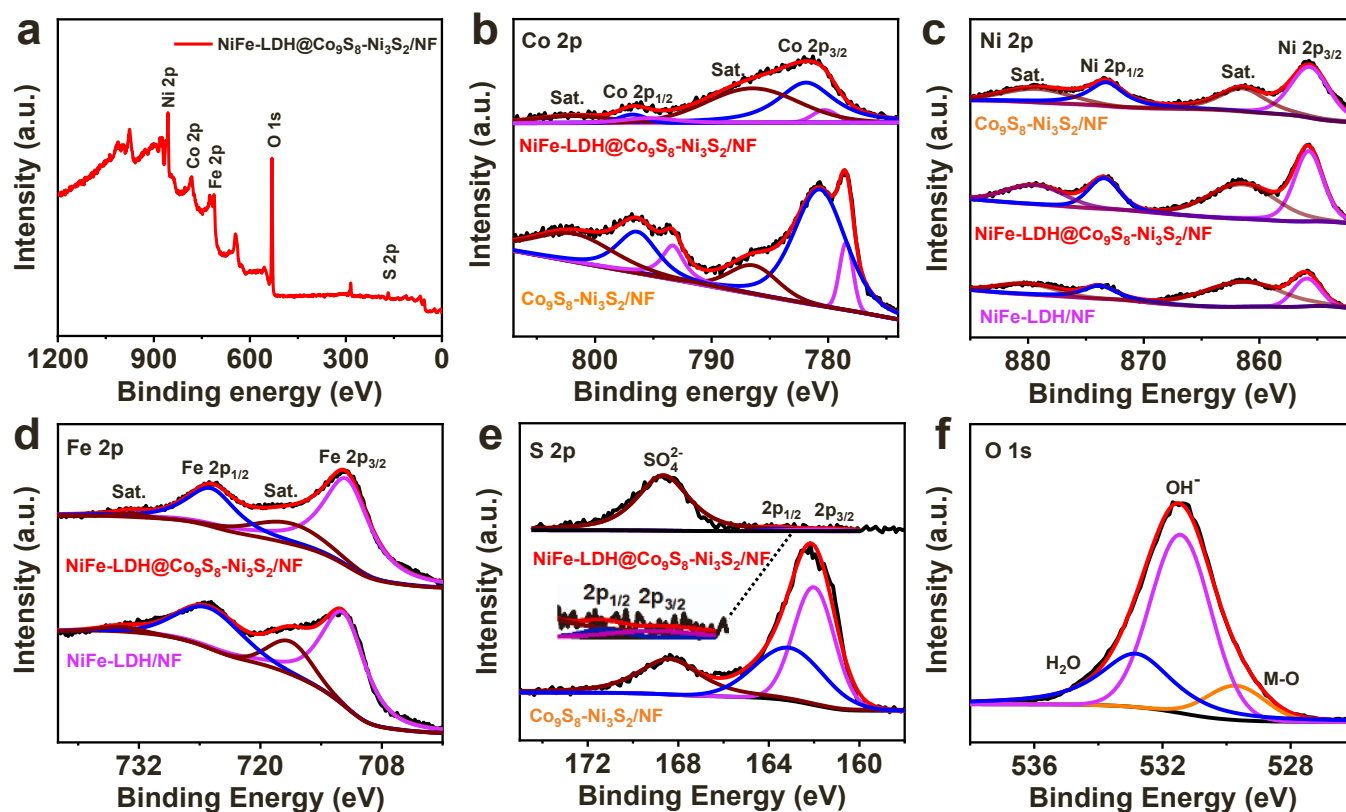

Fig. 4. (a) XPS survey spectrum of NiFe-LDH@Co$_9$S$_8$-Ni$_3$S$_2$/NF, (b) Co 2p spectra of NiFe-LDH@Co$_9$S$_8$-Ni$_3$S$_2$/NF and Co$_9$S$_8$-Ni$_3$S$_2$/NF, (c) Ni 2p spectra of NiFe-LDH@Co$_9$S$_8$-Ni$_3$S$_2$/NF, Co$_9$S$_8$-Ni$_3$S$_2$/NF and NiFe-LDH/NF, (d) Fe 2p spectra of NiFe-LDH@Co$_9$S$_8$-Ni$_3$S$_2$/NF and NiFe-LDH/NF, (e) S 2p spectra of NiFe-LDH@Co$_9$S$_8$-Ni$_3$S$_2$/NF and Co$_9$S$_8$-Ni$_3$S$_2$/NF and (f) O 1 s spectra of NiFe-LDH@Co$_9$S$_8$-Ni$_3$S$_2$/NF.

Supplementary material related to this article can be found online at doi:10.1016/j.apcatb.2024.124140.

3.2. OER performance in alkaline freshwater

The OER performance of NiFe-LDH@Co$_9$S$_8$-Ni$_3$S$_2$/NF along with control samples was first evaluated in a 1 M KOH. Considering the possible influence of halogen on the morphology and activity of the
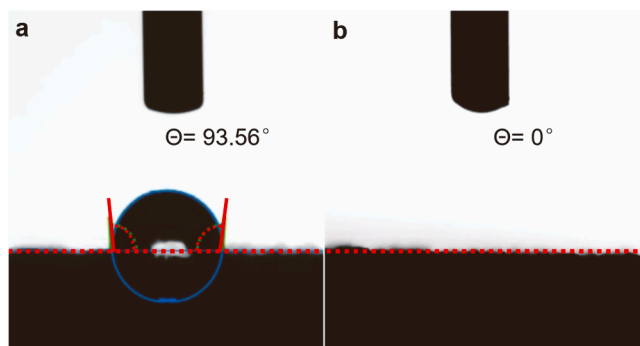
Fig. 5. Contact angles of (a) NF and (b) NiFe-LDH@Co$_9$S$_8$-Ni$_3$S$_2$/NF with freshwater.

resulting electrocatalysts [46–48], the OER activities of Ni-Co precursor/NF synthesized by adding different ammonium halides (NH$_4$F, NH$_4$Cl, and NH$_4$Br) were first explored. The corresponding LSV curves confirm that the Ni-Co precursor/NF synthesized by adding NH$_4$F has the best OER activity at large current densities (Fig. S5). This may be attributed to its distinct structure, which is favorable for mass transfer (Fig. S6). Afterwards, various synthesis conditions, such as hydrothermal reaction time, temperatures, Ni-Co ratios and electrodeposition time were first explored (Fig. S7). Subsequently, the performance of NiFe-LDH@Co$_9$S$_8$-Ni$_3$S$_2$/NF and control samples was further evaluated. The measured LSV curves (Fig. 6a) demonstrate that bare NF has inadequate OER activity, whereas NiFe-LDH/NF and Co$_9$S$_8$-Ni$_3$S$_2$/NF possess moderate OER activity. In contrast, NiFe-LDH@Co$_9$S$_8$-Ni$_3$S$_2$/NF displays admirable OER activity, achieving 100 mA cm^{-2} with a low overpotential of 223 mV. This value outperforms that of NiFe-LDH/NF, Co$_9$S$_8$-Ni$_3$S$_2$/NF and IrO$_2$/NF with optimized loading amount (Fig. S8). This significantly enhanced activity for NiFe-LDH@Co$_9$S$_8$-Ni$_3$S$_2$/NF highlights the crucial role played by the formation of heterostructures and the collaborative impact between NiFe-LDH and Co$_9$S$_8$-Ni$_3$S$_2$. Moreover, it is noteworthy that 500 and 1000 mA cm^{-2} are commonly employed in industrial applications, NiFe-LDH@Co$_9$S$_8$-Ni$_3$S$_2$/NF only necessitates small overpotentials of 260 and 274 mV, respectively, implying its potential for industrial applications (Fig. 6b). The Tafel slope, serving as an indicator of the reaction kinetics, was further analyzed. Compared with NiFe-LDH/NF (70.71 mV dec^{-1}) and Co$_9$S$_8$-Ni$_3$S$_2$/NF (75.17 mV dec^{-1}), NiFe-LDH@Co$_9$S$_8$-Ni$_3$S$_2$/NF displays the smallest Tafel slope of 36.44 mV dec^{-1}, revealing its fastest reaction kinetics (Fig. 6c). In order to explore the possibility of an enhanced mechanism of NiFe-LDH@Co$_9$S$_8$-Ni$_3$S$_2$/NF, CV scanning was conducted to obtain the C_{dl} (Fig. S9), which is positively correlated with ECSA. The obtained C_{dl} value for NiFe-LDH@Co$_9$S$_8$-Ni$_3$S$_2$/NF is 22.76 mF cm^{-2} (Fig. 6d), larger than that of NiFe-LDH/NF (4.19 mF cm^{-2}) and Co$_9$S$_8$-Ni$_3$S$_2$/NF (12.35 mF cm^{-2}). The largest C_{dl} value for NiFe-LDH@Co$_9$S$_8$-Ni$_3$S$_2$/NF reveals its most abundant active sites. Moreover, after normalizing the LSV current by ECSA, the NiFe-LDH@Co$_9$S$_8$-Ni$_3$S$_2$/NF also displays the highest intrinsic activity, as demonstrated by its largest specific current density among the as-fabricated samples (Fig. 6e). Therefore, the outstanding OER activity should stem from the increased number of activity sites and enhanced intrinsic activity achieved through heterostructure formation.

The charge transfer kinetics significantly influence the activity of an electrocatalyst, which was analyzed using EIS and the corresponding charge transfer resistance (R_{ct}) was determined by fitting Nyquist plots by equivalent circuit fitting (Fig. 6f and S10). Among the as-fabricated samples, NiFe-LDH@Co$_9$S$_8$-Ni$_3$S$_2$/NF exhibits the smallest R_{ct} value of 0.22 Ω compared to Co$_9$S$_8$-Ni$_3$S$_2$/NF (0.33 Ω) and NiFe-LDH/NF (0.30 Ω), revealing superior charge transfer kinetics for NiFe-LDH@Co$_9$S$_8$-Ni$_3$S$_2$/NF. Furthermore, EIS measurements were performed under different potentials to analyze the charge transfer properties under

different potentials (Fig. S11a-c). It is evident that NiFe-LDH@Co$_9$S$_8$-Ni$_3$S$_2$/NF always maintains a minimum R_{ct} value as the voltage increases (Fig. 6g), indicating its fastest charge transfer kinetics. Additionally, the Bode plots of the three as-fabricated samples all display a distinct transition peak at each potential, corresponding to the OER process. Notably, these transition peaks gradually diminish as the potential increases, indicating an accelerated OER process (Fig. S11d-f). Besides, NiFe-LDH@Co$_9$S$_8$-Ni$_3$S$_2$/NF consistently exhibits the lowest phase angle of the transition peak, providing further evidence of its exceptional charge transfer kinetics (Fig. 6h).

The electrocatalyst usually undergoes oxidization to form oxyhydroxide during the OER process, which is commonly considered the real OER active species. Therefore, the redox properties of the as-fabricated samples were investigated through CV. As presented in Fig. S12a-c, the CV curves for thee as-fabricated samples without *iR* compensation also exhibit distinct redox peaks corresponding to the valance state change of active sites. The redox reaction kinetics of different samples can be analyzed through the equation $i_p=av^b$, where i_p is peak current desnity (mA cm^{-2}), v represents scan speed (mV s^{-1}) and value of b can be determined by fitting log$i$ against log$v$. When b is closer to 1, the reaction is predominantly influenced by capacitance behavior; conversely, when b tends towards 0.5, diffusion becomes the dominant controlling factor [49,50]. The fitted b values of NiFe-LDH@Co$_9$S$_8$-Ni$_3$S$_2$/NF, Co$_9$S$_8$-Ni$_3$S$_2$/NF and NiFe-LDH/NF are 0.674, 0.634 and 0.565 (Fig. 6i), respectively. A range between 0.5 and 1 indicates that NiFe-LDH@Co$_9$S$_8$-Ni$_3$S$_2$/NF and Co$_9$S$_8$-Ni$_3$S$_2$/NF are affected by both capacitance behavior and diffusion control, and NiFe-LDH/NF is mainly affected by diffusion. The diffusion-controlled behavior of the electrocatalyst may result from either concentration polarization or mass transport [49]. The larger b value of NiFe-LDH@Co$_9$S$_8$-Ni$_3$S$_2$/NF illustrates the improved reaction kinetics due to the formation heterostructure. Besides, the higher peak current density of NiFe-LDH@Co$_9$S$_8$-Ni$_3$S$_2$/NF compared to that of Co$_9$S$_8$-Ni$_3$S$_2$/NF and NiFe-LDH/NF at the same sweep speed also demonstrates the promoted redox reaction resulting from the addition of NiFe-LDH (Fig. S12d). Therefore, the OER activity of NiFe-LDH@Co$_9$S$_8$-Ni$_3$S$_2$/NF was improved.

The stability of electrocatalysts is a crucial benchmark for assessing their performance. The durability of NiFe-LDH@Co$_9$S$_8$-Ni$_3$S$_2$/NF was initially evaluated through CV measurement. The LSV curve after 5000 CV scans showed little change from the initial curves (Fig. S13a). Moreover, the CP measurements demonstrate that NiFe-LDH@Co$_9$S$_8$-Ni$_3$S$_2$/NF possesses exceptional stability at 100 mA cm^{-2} (Fig. S13b) and 500 mA cm^{-2} (Fig. 6j). Following OER testing, NiFe-LDH@Co$_9$S$_8$-Ni$_3$S$_2$/NF was subjected to XRD, SEM, and XPS characterization to analyze the evolution of its composition, morphology and structure. The corresponding XRD patterns indicate that there is no significant change observed except for a weakening in peak intensity (Fig. S14), which may be caused by the surface reconstruction. Nevertheless, the primal morphology of NiFe-LDH@Co$_9$S$_8$-Ni$_3$S$_2$/NF remains predominantly unaltered (Fig. S15). Further TEM characterization demonstrates excellent preservation of the heterostructure of NiFe-LDH@Co$_9$S$_8$-Ni$_3$S$_2$/NF (Fig. S16a). The face spacing of 0.220 and 0.245 nm is consistent with the (101) plane of Co$_9$S$_8$ and the (202) plane of Ni$_3$S$_2$ (Fig. S16b), respectively. Furthermore, the elemental distribution analysis clearly reveals the even distribution of various elements (Fig. S16c). Notably, the percentage of O element is a significant increase compared to the original sample (Fig. S17), which may be attributed to the surface reconstruction forming oxyhydroxide. After long-term OER testing, the ratio of Co^{3+}/Co^{2+} increases to 0.75 from 0.21 (Fig. S18a), demonstrating an increase in the amount of CoOOH [51]. Regarding the Ni 2p spectra after long-term OER test (Fig. S18b), two peaks at 856.73 eV and 874.67 eV indicate the presence of Ni^{3+} [52]. Additionally, both peaks corresponding to Ni 2p$_{1/2}$ and Ni 2p$_{3/2}$ positively shift towards higher binding energy, further confirming the generation of Ni^{3+} resulting from the partial oxidation of Ni^{2+} [38]. As for the Fe 2p spectra (Fig. S18c),
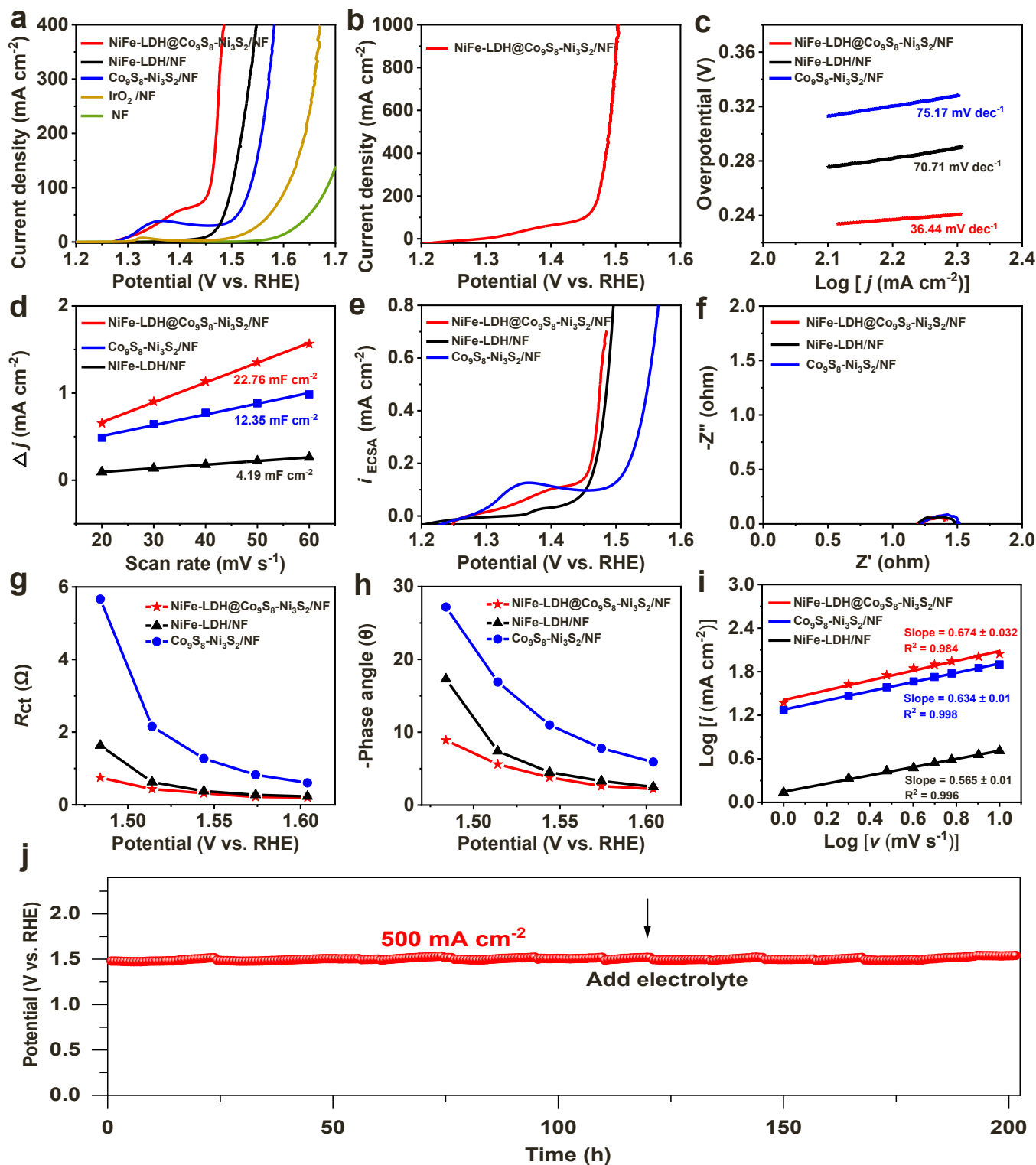
Fig.6. OER performance of different electrocatalysts in 1 M KOH solution: (a) LSV curves, (b) LSV curve of NiFe-LDH@Co$_9$S$_8$-Ni$_3$S$_2$/NF with high current density, (c) Tafel slopes, (d) C_{dl}, (e) LSV curves of current density normalized by ECSA, (f) Nyquist plots, (g) R_{ct} values under different potentials, (h) Phase angle values under different potentials, (i) Linear fitting plots of logi_p and log$v$ and (j) Stability test at 500 mA cm^{-2}.

there is no noticeable alteration observed in comparison to its pre-OER test state. As for the S 2p spectra (Fig. S18d), no peak associated with the S element was observed, indicating the leaching of S resulting from the reconstruction of the electrocatalyst [53]. In addition, the content of the S element was observably in the electrolyte after long-term OER test (Fig. S19a), again demonstrating the leaching of the S element. As for

the metal element, only slight leaching was observed (Fig. S19b-d). In light of the aforementioned findings, we can deduce that NiFe-LDH@-Co$_9$S$_8$-Ni$_3$S$_2$/NF undergoes surface reconstruction to form oxyhydroxide, which is commonly considered the active species for OER [54].

Additionally, the exceptional activity and durability exhibited by

NiFe-LDH@Co$_9$S$_8$-Ni$_3$S$_2$/NF surpass that of many recently reported OER electrocatalysts, demonstrating its promising prospects as a superior OER electrocatalyst (Table S1). To assess the feasibility of utilizing NiFe-LDH@Co$_9$S$_8$-Ni$_3$S$_2$/NF as an OER electrocatalyst for practical applications, an electrolytic cell using Pt/C as the HER electrocatalyst and NiFe-LDH@Co$_9$S$_8$-Ni$_3$S$_2$/NF as the OER electrocatalyst was assembled in 1 M KOH. As depicted in Fig. 7a, Pt/C/NF || NiFe-LDH@Co$_9$S$_8$-Ni$_3$S$_2$/NF only needs voltages of 1.51, 1.64, and 1.72 V at 100, 500, and 1000 mA cm^{-2}, which confirms its potential as a highly active OER electrocatalyst. In addition, the volume of generated O$_2$ is in accordance with the theoretical values, demonstrating that the electrolyzer's overall freshwater splitting process operates at a Faraday efficiency of close to 99 % (Fig. 7b and c).

To gain a deep understanding of the impact of heterostructure formation on the enhanced OER activity, the pH-dependence of the OER activity was further investigated to explore the OER pathway. As presented in Fig. S20a-c, the OER activities of NiFe-LDH@Co$_9$S$_8$-Ni$_3$S$_2$/NF, Co$_9$S$_8$-Ni$_3$S$_2$/NF, and NiFe-LDH/NF all decrease with decreasing pH. Notably, NiFe-LDH@Co$_9$S$_8$-Ni$_3$S$_2$/NF exhibits the most significant degradation in OER activity. To establish a clear correlation between the OER activity and pH, the proton reaction orders on the RHE scale were calculated according to the equation: $\rho_{RHE}=\partial log j/\partial pH$ [55]. The calculated values of ρ_{RHE} for NiFe-LDH@Co$_9$S$_8$-Ni$_3$S$_2$/NF, Co$_9$S$_8$-Ni$_3$S$_2$/NF, and NiFe-LDH/NF are 0.52, 0.30, and 0.40, respectively (Fig. S20d). The highest ρ_{RHE} value for NiFe-LDH@Co$_9$S$_8$-Ni$_3$S$_2$/NF indicates that it may undergo the LOM pathway rather than the AEM pathway. Unlike the AEM pathway, the LOM pathway will generate O$_2^{2-}$, therefore, detecting the presence of O$_2^{2-}$ is an important indicator of the LOM pathway [56,57]. Tetramethylammonium cation (TMA$^+$) exhibits strong binding strength with O$_2^{2-}$, which was used as a probe to detect the presence of O$_2^{2-}$ [55,58]. The corresponding results revealed that the OER activity of NiFe-LDH@Co$_9$S$_8$-Ni$_3$S$_2$/NF exhibits a more significant decrease in 1 M TMAOH in comparison with Co$_9$S$_8$-Ni$_3$S$_2$/NF and NiFe-LDH/NF (Fig. S21). This again demonstrated that the formation of heterostructure can trigger more lattice oxygen to participate in the LOM process, thus leading to an obviously enhanced OER activity of NiFe-LDH@Co$_9$S$_8$-Ni$_3$S$_2$/NF [59].

3.3. OER performance in alkaline seawater

Considering the overpotential at 1000 mA cm^{-2} is only 274 mV in 1 M KOH, which is significantly smaller than 480 mV and can effectively avoid hypochlorite formation [60,61]. This indicates its high potential as an appropriate electrocatalyst for the electrolysis of seawater. Therefore, the OER activity of NiFe-LDH@Co$_9$S$_8$-Ni$_3$S$_2$/NF in alkaline simulated seawater (1 M KOH + 0.5 M NaCl) and alkaline seawater (1 M KOH) was further evaluated. As presented in Fig. 8a and b, NiFe-LDH@Co$_9$S$_8$-Ni$_3$S$_2$/NF still has excellent OER activity in alkaline simulated seawater and alkaline seawater. In the case of alkaline simulated seawater, NiFe-LDH@Co$_9$S$_8$-Ni$_3$S$_2$/NF can drive 100, 500 and 1000 mA cm^{-2} at remarkably low overpotentials of only 227, 274 and 287 mV, respectively. Similarly, in alkaline seawater, to drive current densities of the same magnitude (100, 500, and 1000 mA cm^{-2}), the overpotentials are 244, 285 and 298 mV, respectively, further confirming the exceptional electrocatalytic properties possessed by NiFe-LDH@Co$_9$S$_8$-Ni$_3$S$_2$/NF. In addition, NiFe-LDH@Co$_9$S$_8$-Ni$_3$S$_2$/NF still has a low Tafel slope in simulated seawater and seawater, which is 45.74 and 46.92 mV dec^{-1}, respectively (Fig. 8c). This proves that NiFe-LDH@Co$_9$S$_8$-Ni$_3$S$_2$/NF maintains superior reaction kinetics in both simulated seawater and seawater. The slightly decreased activity in seawater is primarily caused by the hindrance of active sites and surface pollution caused by ions or particles in the seawater [26,62]. Moreover, the activity of NiFe-LDH@Co$_9$S$_8$-Ni$_3$S$_2$/NF in alkaline seawater also surpasses that of many recently reported OER electrocatalysts in the same environment (Fig. 8d and Table S2). Furthermore, NiFe-LDH@Co$_9$S$_8$-Ni$_3$S$_2$/NF can still maintain a stability of 200 h at 500 mA cm^{-2}, with only a slightly increased potential, confirming its excellent stability in alkaline seawater (Fig. 8e). This exceptional stability surpasses that observed in many recently reported OER electrocatalysts (Table S2). Moreover, the assembled Pt/C/NF || NiFe-LDH@Co$_9$S$_8$-Ni$_3$S$_2$/NF also demonstrates remarkable activity for seawater splitting (Fig. S22), as evidenced by its low voltages of only 1.53, 1.66, and 1.76 V to achieve 100, 500, and 1000 mA cm^{-2}, respectively. These findings further validate the potential of NiFe-LDH@Co$_9$S$_8$-Ni$_3$S$_2$/NF as a highly efficient OER electrocatalyst for seawater splitting.

After the long-term OER test in alkaline seawater, the corresponding XRD patterns of NiFe-LDH@Co$_9$S$_8$-Ni$_3$S$_2$/NF showed no change except
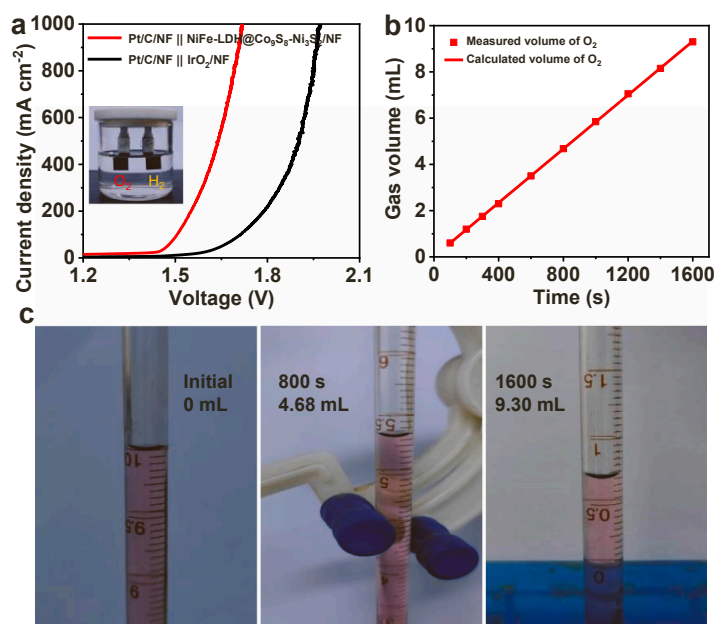

Fig. 7. (a) LSV curves of Pt/C/NF || NiFe-LDH@Co$_9$S$_8$-Ni$_3$S$_2$/NF and Pt/C/NF || IrO$_2$/NF in 1 M KOH and the corresponding digital photographs of Pt/C/NF || NiFe-LDH@Co$_9$S$_8$-Ni$_3$S$_2$/NF, (b) Volume of collected O$_2$ as a function of time and (c) Digital photographs showcasing the O$_2$ volume at different test time.
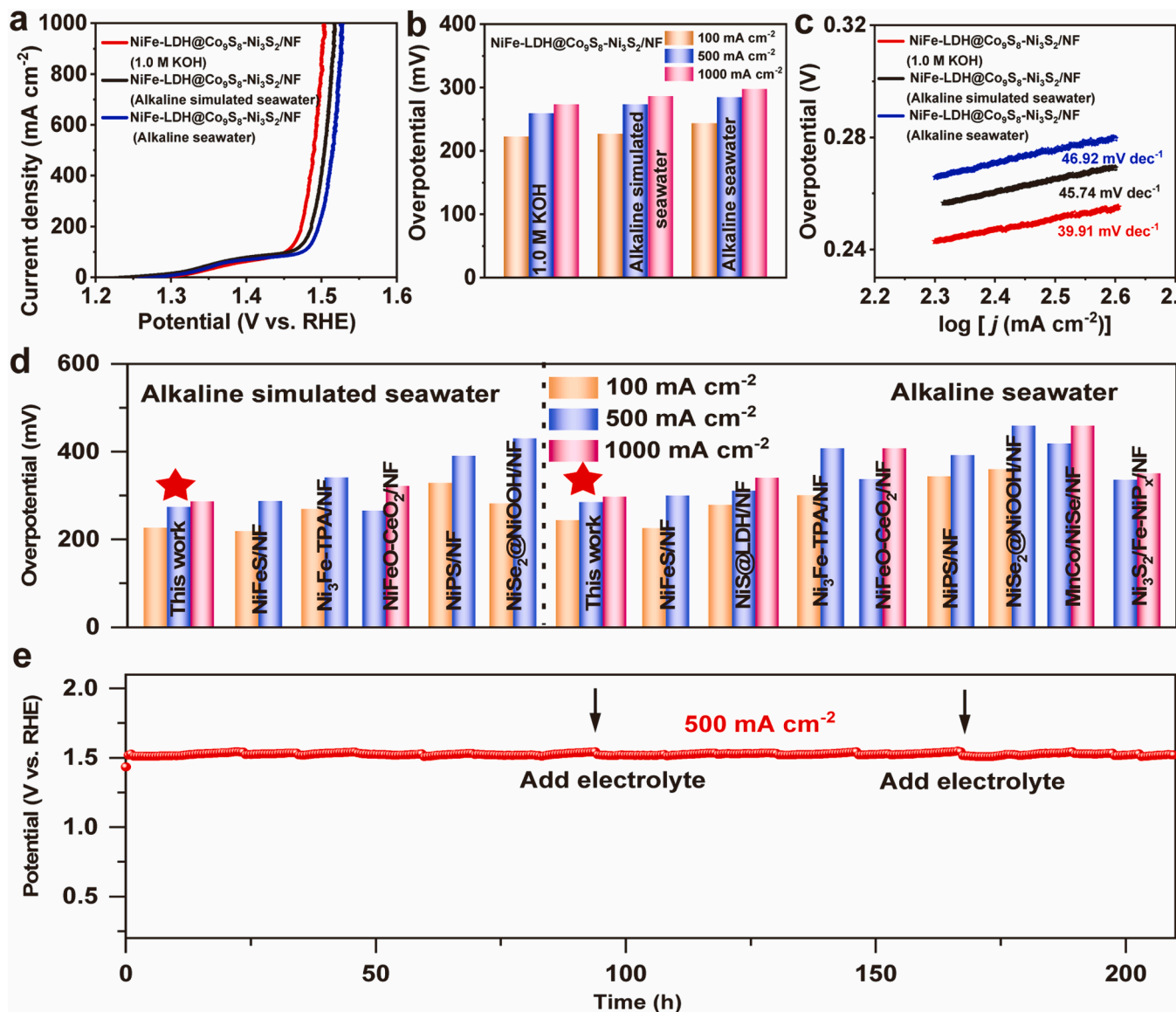
Fig.8. (a) The comparison of the LSV curves collected in different electrolytes, (b) Overpotential diagrams in different electrolytes, (c) Tafel slopes and (d) The comparison of the overpotential of NiFe-LDH@Co$_9$S$_8$-Ni$_3$S$_2$/NF with other reported electrocatalysts. (e) Stability test in alkaline seawater.

for a decrease in the peak intensity (Fig. S23). NiFe-LDH@Co$_9$S$_8$-Ni$_3$S$_2$/NF still maintains the original rod-like structure (Fig. S24), while the morphology of the nanosheet becomes less apparent compared to that observed after long-term OER testing in 1 M KOH. This can be attributed to the corrosion caused by Cl$^-$ in seawater. Further TEM characterization revealed the presence of nanosheets, but their size was reduced due to seawater corrosion (Fig. S25a). The observed facet spacing of 0.175 and 0.245 nm is consistent with the (222) facet of Co$_9$S$_8$ and the (202) facet of Ni$_3$S$_2$, respectively (Fig. S25b). The EDX mapping images, element spectra, and ICP-MS analysis reveal a slightly more pronounced leaching of S and Fe elements in alkaline seawater after long-term OER test due to the corrosion caused by Cl$^-$ ions (Fig. S26-S28). Additionally, the XPS analysis demonstrates that no significant difference was observed compared with that observed after the long-term OER test in 1 M KOH, except that the peak intensity decreased (Fig. S29). This can be attributed to the precipitate formation on the surface of NiFe-LDH@Co$_9$S$_8$-Ni$_3$S$_2$/NF, as demonstrated by the presence of Ca^{2+} and Mg^{2+} ions based on the EDX spectra analysis (Fig. S27).

4. Conclusions

In summary, a high-efficiency and durable OER electrocatalyst in alkaline freshwater and alkaline seawater, heterostructured NiFe-LDH@Co$_9$S$_8$-Ni$_3$S$_2$/NF was designed and synthesized through the hydrothermal method combined with electrodeposition. The heterostructure consists of Co$_9$S$_8$-Ni$_3$S$_2$ nanorods and NiFe-LDH nanosheets. Due to the formation of heterostructures with the abundance of exposed active sites, excellent wettability, efficient interfacial charge transfer, fast mass transport, and tunable electronic structure, the optimized NiFe-LDH@Co$_9$S$_8$-Ni$_3$S$_2$/NF displays superior OER activity with remarkably low overpotentials of 274 mV in alkaline freshwater and 298 mV in alkaline seawater at 1000 mA cm^{-2}. Furthermore, NiFe-LDH@Co$_9$S$_8$-Ni$_3$S$_2$/NF also demonstrates outstanding stability over 200 h at 500 mA cm^{-2} in both alkaline freshwater and alkaline seawater. Our present work provides valuable insights for designing high-performance OER electrocatalysts for industrial electrolysis of seawater.

CRediT authorship contribution statement

Liying Liu: Writing – original draft, Methodology, Formal analysis, Data curation, Conceptualization. **Yangyang Chen:** Visualization, Investigation, Data curation. **Qi Zhang:** Investigation, Formal analysis. **Zhe Liu:** Resources, Funding acquisition, Formal analysis. **Kefen Yue:** Writing – review & editing, Supervision, Resources, Project administration, Funding acquisition, Conceptualization. **Yongliang Cheng:** Writing – review & editing, Supervision, Project administration, Funding acquisition, Conceptualization. **Dongsheng Li:** Writing – review & editing, Funding acquisition. **Zhonghua Zhu:** Writing – review & editing. **Jiayao Li:** Visualization, Investigation, Funding acquisition. **Yaoyu Wang:** Writing – review & editing.

Declaration of Competing Interest

The authors declare that they have no known competing financial interests or personal relationships that could have appeared to influence the work reported in this paper.

Data availability

Data will be made available on request.

Acknowledgements

Appendix A. Supporting information

Supplementary data associated with this article can be found in the online version at doi:10.1016/j.apcatb.2024.124140.

References

[1] Z.W. Seh, J. Kibsgaard, C.F. Dickens, I.B. Chorkendorff, J.K. Norskov, T. F. Jaramillo, Combining theory and experiment in electrocatalysis: insights into materials design, Science 355 (2017) eaad4998.

[2] X. Zou, Y. Zhang, Noble metal-free hydrogen evolution catalysts for water splitting, Chem. Soc. Rev. 44 (2015) 5148–5180.

[3] L. Bian, Z.-Y. Zhang, H. Tian, N.-N. Tian, Z. Ma, Z.-L. Wang, Grain boundary-abundant copper nanoribbons on balanced gas-liquid diffusion electrodes for efficient CO_2 electroreduction to C_2H_4, Chin. J. Catal. 54 (2023) 199–211.

[4] Z.-Y. Zhang, H. Tian, H. Jiao, X. Wang, L. Bian, Y. Liu, N. Khaorapapong, Y. Yamauchi, Z.-L. Wang, SiO_2 assisted Cu^0-Cu^+-NH_2 composite interfaces for efficient CO_2 electroreduction to C_{2+} products, J. Mater. Chem. A 12 (2024) 1218–1232.

[5] J. Hu, C. Zhang, X. Meng, H. Lin, C. Hu, X. Long, S. Yang, Hydrogen evolution electrocatalysis with binary-nonmetal transition metal compounds, J. Mater. Chem. A 5 (2017) 5995–6012.

[6] G. Zhao, Y. Jiang, S.-X. Dou, W. Sun, H. Pan, Interface engineering of heterostructured electrocatalysts towards efficient alkaline hydrogen electrocatalysis, Sci. Bull. 66 (2021) 85–96.

[7] C.-F. Li, L.-J. Xie, J.-W. Zhao, L.-F. Gu, J.-Q. Wu, G.-R. Li, Interfacial electronic modulation by Fe_2O_3/NiFe-LDHs heterostructures for efficient oxygen evolution at high current density, Appl. Catal. B-Environ. 306 (2022) 121097.

[8] W. Zhang, D. Li, L. Zhang, X. She, D. Yang, NiFe-based nanostructures on nickel foam as highly efficiently electrocatalysts for oxygen and hydrogen evolution reactions, J. Energy Chem. 39 (2019) 39–53.

[9] X.-W. Chang, S. Li, L. Wang, L. Dai, Y.-P. Wu, X.-Q. Wu, Y. Tian, S. Zhang, D.-S. Li, Tuning morphology and electronic structure of cobalt metaphosphate via vanadium-doping for efficient water and urea splitting, Adv. Funct. Mater. (2024) 2313974.

[10] Z. Liu, B. Tang, X. Gu, H. Liu, L. Feng, Selective structure transformation for NiFe/$NiFe_2O_4$ embedded porous nitrogen-doped carbon nanosphere with improved oxygen evolution reaction activity, Chem. Eng. J. 395 (2020) 125170.

[11] K. Zhu, F. Shi, X. Zhu, W. Yang, The roles of oxygen vacancies in electrocatalytic oxygen evolution reaction, Nano Energy 73 (2020) 104761.

[12] L. Lin, Y. Wang, Q. Ye, Y. Zhao, Y. Cheng, Rapid fabrication of $Fe_xNi_{2-x}P_4O_{12}$ and graphene hybrids as electrocatalyst for highly efficient oxygen evolution reaction, Appl. Catal. B-Environ. (2023) 122834.

[13] P. Wang, X. Zhang, J. Zhang, S. Wan, S. Guo, G. Lu, J. Yao, X. Huang, Precise tuning in platinum-nickel/ nickel sulfide interface nanowires for synergistic hydrogen evolution catalysis, Nat. Commun. 8 (2017) 14580.

[14] H. Jin, S. Choi, G.J. Bang, T. Kwon, H.S. Kim, S.J. Lee, Y. Hong, D.W. Lee, H. S. Park, H. Baik, Y. Jung, S.J. Yoo, K. Lee, Safeguarding the RuO_2 phase against lattice oxygen oxidation during acidic water electrooxidation, Energy Environ. Sci. 15 (2022) 1119–1130.

[15] W. Sun, L.-m Cao, J. Yang, Conversion of inert cryptomelane-type manganese oxide into a highly efficient oxygen evolution catalyst via limited Ir doping, J. Mater. Chem. A 4 (2016) 12561–12570.

[16] B. Weng, F. Xu, C. Wang, W. Meng, C.R. Grice, Y. Yan, A layered $Na_{1-x}Ni_yFe_{1-y}O_2$ double oxide oxygen evolution reaction electrocatalyst for highly efficient water-splitting, Energy Environ. Sci. 10 (2017) 121–128.

[17] J.-Y. Luo, Y. Yuan, H.-Y. Ruan, X.-Q. Wu, Y.-P. Wu, S. Li, G. Zhang, S. Sun, D.-S. Li, Electrochemical reconstruction engineering: metal-organic gels as pre-catalysts for NiOOH/FeOOH heterostructure to boost oxygen evolution reaction, Small Struct. 4 (2023) 2300074.

[18] L. Wei, M. Du, R. Zhao, F. Lv, L. Li, L. Zhang, D. Zhou, J. Su, High-valence Mo doping for highly promoted water oxidation of NiFe (oxy)hydroxide, J. Mater. Chem. A 10 (2022) 23790–23798.

[19] P.P. Dhakal, U.N. Pan, D.R. Paudel, M.R. Kandel, N.H. Kim, J.H. Lee, Cobalt-manganese sulfide hybridized Fe-doped 1T-Vanadium disulfide 3D-Hierarchical core-shell nanorods for extreme low potential overall water-splitting, Mater. Today Nano 20 (2022) 100272.

[20] X. Jia, H. Kang, X. Yang, Y. Li, K. Cui, X. Wu, G. Wu, Amorphous Ni(III)-based sulfides as bifunctional water and urea oxidation anode electrocatalysts for hydrogen generation from urea-containing water, Appl. Catal. B Environ. 312 (2022) 121389.

[21] Y. Zhang, M. Chen, P. Guo, Y. Du, B. Song, X. Wang, Z. Jiang, P. Xu, Magnetic field-enhanced water splitting enabled by bifunctional molybdenum-doped nickel sulfide on nickel foam, Carbon Energy 5 (2023) e351.

[22] X. Shen, H. Li, Y. Zhang, T. Ma, Q. Li, Q. Jiao, Y. Zhao, H. Li, C. Feng, Construction dual-regulated $NiCo_2S_4$ @Mo-doped CoFe-LDH for oxygen evolution reaction at large current density, Appl. Catal. B-Environ. 319 (2022) 121917.

[23] W. Ma, D. Li, L. Liao, H. Zhou, F. Zhang, X. Zhou, Y. Mo, F. Yu, High-performance bifunctional porous iron-rich phosphide/nickel nitride heterostructures for alkaline seawater splitting, Small 19 (2023) 2207082.

[24] Z. Zhao, J. Sun, X. Li, Z. Zhang, X. Meng, Joule heating synthesis of NiFe alloy/MoO_2 and in-situ transformed (Ni,Fe)OOH/MoO_2 heterostructure as effective complementary electrocatalysts for overall splitting in alkaline seawater, Appl. Catal. B-Environ. 340 (2024) 123277.

[25] S.A. Patil, A.C. Khot, V.D. Chavan, I. Rabani, D.-k Kim, J. Jung, H. Im, N. K. Shrestha, Electrostatically robust CoFeOF nanosheet against chloride for green-H2 production in alkaline seawater electrolysis, Chem. Eng. J. 480 (2024) 146545.

[26] S. Zhou, J. Wang, J. Li, L. Fan, Z. Liu, J. Shi, W. Cai, Surface-growing organophosphorus layer on layered double hydroxides enables boosted and durable electrochemical freshwater/seawater oxidation, Appl. Catal. B Environ. 332 (2023) 122749.

[27] X. Yu, Z.-Y. Yu, X.-L. Zhang, Y.-R. Zheng, Y. Duan, Q. Gao, R. Wu, B. Sun, M.-R. Gao, G. Wang, S.-H. Yu, Superaerophobic" nickel phosphide nanoarray catalyst for efficient hydrogen evolution at ultrahigh current densities, J. Am. Chem. Soc. 141 (2019) 7537–7543.

[28] L. Yang, D. Lu, L. Zhao, D. Xia, Construction of Mo doped CoMoCH-Cu2SeS/NF composite electrocatalyst with high catalytic activity and corrosion resistance in seawater electrolysis: a case study on cleaner energy, J. Clean. Prod. 413 (2023) 137462.

[29] Y.-j Wu, J. Yang, T.-x Tu, W.-q Li, P.-f Zhang, Y. Zhou, J.-f Li, J.-t Li, S.-G. Sun, Evolution of cationic vacancy defects: a motif for surface restructuration of OER precatalyst, Angew. Chem. Int. Ed. 60 (2021) 26829–26836.

[30] Y. Zhai, X. Ren, Y. Sun, D. Li, B. Wang, S. Liu, Synergistic effect of multiple vacancies to induce lattice oxygen redox in NiFe-layered double hydroxide OER catalysts, Appl. Catal. B-Environ. 323 (2023) 122091.

[31] M. Qin, Y. Li, H. Zhang, M. Humayun, X. Xu, Y. Fu, M.K. Kadirov, C. Wang, Crystalline/amorphous heterostructure offering highly efficient overall water splitting and urea electrolysis, J. Alloy. Compd. 921 (2022) 166071.

[32] M.A. Djebbi, S. Boubakri, M. Braiek, N. Jaffrezic-Renault, Pe Namour, A.B. H. Amara, Chlorpromazine electro-oxidation at BDD electrode modified with nZVI nanoparticles impregnated NiAl LDH, Electroanalysis 32 (2020) 1186–1197.

[33] L.B. Staal, S.S.C. Pushparaj, C. Forano, V. Prevot, D.B. Ravnsbaek, M. Bjerring, U. G. Nielsen, Competitive reactions during synthesis of zinc aluminum layered double hydroxides by thermal hydrolysis of urea, J. Mater. Chem. A 5 (2017) 21795–21806.

[34] W. Chen, C. Chen, L. Li, Z. Lin, Partial carbonization and etching of ZIF-9 to construct SO_4^{2-}-decorated C@NiCoFe LDH ultrathin nanosheets for efficient oxygen evolution reaction, J. Mater. Chem. A 11 (2023) 11170–11178.

[35] Z. Pan, Z. Tang, D. Sun, Y. Zhan, Hierarchical $NiCo_2S_4$@$NiMoO_4$ nanotube arrays on nickel foam as an advanced bifunctional electrocatalyst for efficient overall water splitting, Electrochim. Acta 436 (2022) 141393.

[36] J. Liu, J. Wang, B. Zhang, Y. Ruan, L. Lv, X. Ji, K. Xu, L. Miao, J. Jiang, Hierarchical $NiCo_2S_4$@NiFe LDH heterostructures supported on nickel foam for enhanced overall-water-splitting activity, ACS Appl. Mater. Interfaces 9 (2017) 15364–15372.

[37] A. Sivanantham, P. Ganesan, S. Shanmugam, Hierarchical NiCo$_2$S$_4$ nanowire arrays supported on Ni Foam: an efficient and durable bifunctional electrocatalyst for oxygen and hydrogen evolution reactions, Adv. Funct. Mater. 26 (2016) 4661–4672.

[38] X. Feng, Q. Jiao, W. Chen, Y. Dang, Z. Dai, S.L. Suib, J. Zhang, Y. Zhao, H. Li, C. Feng, Cactus-like NiCo$_2$S$_4$@NiFe LDH hollow spheres as an effective oxygen bifunctional electrocatalyst in alkaline solution, Appl. Catal. B-Environ. 286 (2021) 119869.

[39] J. Yuan, X. Cheng, C. Lei, B. Yang, Z. Li, K. Luo, K.H.K. Lam, L. Lei, Y. Hou, K. K. Ostrikov, Bimetallic oxyhydroxide as a high-performance water oxidation electrocatalyst under industry-relevant conditions, Engineering 7 (2021) 1306–1312.

[40] H.-S. Hu, S. Si, R.-J. Liu, C.-B. Wang, Y.-Y. Feng, Iron-nickel hydroxide nanoflake arrays supported on nickel foam with dramatic catalytic properties for the evolution of oxygen at high current densities, Int. J. Energy Res. 44 (2020) 9222–9232.

[41] Y. Lu, C. Liu, Y. Xing, Q. Xu, A.M.S. Hossain, D. Jiang, D. Li, J. Zhu, Synergistically integrated Co$_9$S$_8$@NiFe-layered double hydroxide core-branch hierarchical architectures as efficient bifunctional electrocatalyst for water splitting, J. Colloid Interface Sci. 604 (2021) 680–690.

[42] Y.J. Lee, S.-K. Park, Metal-organic framework-derived hollow CoS$_x$ nanoarray coupled with NiFe layered double hydroxides as efficient bifunctional electrocatalyst for overall water splitting, Small 18 (2022) 2200586.

[43] M. Luo, Z. Cai, C. Wang, Y. Bi, L. Qian, Y. Hao, L. Li, Y. Kuang, Y. Li, X. Lei, Z. Huo, W. Liu, H. Wang, X. Sun, X. Duan, Phosphorus oxoanion-intercalated layered double hydroxides for high-performance oxygen evolution, Nano Res. 10 (2017) 1732–1739.

[44] Z. Gu, X. Wei, X. Zhang, Z. Duan, Z. Gu, Q. Gong, K. Luo, Bimetallic-MOF-derived amorphous zinc/cobalt-iron-based hollow nanowall arrays via Ion exchange for highly efficient oxygen evolution, Small 17 (2021) 2104125.

[45] W. Li, M. Chen, Y. Lu, P. Qi, G. Liu, Y. Zhao, H. Wu, Y. Tang, One-pot electrodeposition synthesis of NiFe-phosphate/phosphide hybrid nanosheet arrays for efficient water splitting, Appl. Surf. Sci. 598 (2022) 153717.

[46] H. Song, M. Wu, Z. Tang, J.S. Tse, B. Yang, S. Lu, Single atom ruthenium-doped CoP/CDs nanosheets via splicing of carbon-dots for robust hydrogen production, Angew. Chem. Int. Ed. 60 (2021) 7234–7244.

[47] H. Song, J. Yu, Z. Tang, B. Yang, S. Lu, Halogen-doped carbon dots on amorphous cobalt phosphide as robust electrocatalysts for overall water splitting, Adv. Energy Mater. 12 (2022) 2102573.

[48] Y. Zhai, B. Zhang, R. Shi, S. Zhang, Y. Liu, B. Wang, K. Zhang, G.I.N. Waterhouse, T. Zhang, S. Lu, Carbon dots as new building blocks for electrochemical energy storage and electrocatalysis, Adv. Energy Mater. 12 (2022) 2103426.

[49] R. Chen, S.-F. Hung, D. Zhou, J. Gao, C. Yang, H. Tao, H.B. Yang, L. Zhang, L. Zhang, Q. Xiong, H.M. Chen, B. Liu, Layered structure causes bulk NiFe layered

double hydroxide unstable in alkaline oxygen evolution reaction, Adv. Mater. 31 (2019) 1903909.

[50] X. Chen, Q. Wang, Y. Cheng, H. Xing, J. Li, X. Zhu, L. Ma, Y. Li, D. Liu, S-doping triggers redox reactivities of both iron and lattice oxygen in FeOOH for low-cost and high-performance water oxidation, Adv. Funct. Mater. 32 (2022) 2112674.

[51] X. Li, Z. Kou, S. Xi, W. Zang, T. Yang, L. Zhang, J. Wang, Porous NiCo$_2$S$_4$/FeOOH nanowire arrays with rich sulfide/hydroxide interfaces enable high OER activity, Nano Energy 78 (2020) 105230.

[52] S. Dutta, A. Indra, Y. Feng, T. Song, U. Paik, Self-supported nickel iron layered double hydroxide-nickel selenide electrocatalyst for superior water splitting activity, ACS Appl. Mater. Interfaces 9 (2017) 33766–33774.

[53] Y. Qian, B. Zhou, Q. Zhang, H. Yang, Rational design of goethite-sulfide nanowire heterojunctions for high current density water splitting, J. Phys. Chem. Lett. 14 (2023) 6709–6718.

[54] L. He, N. Wang, M. Xiang, L. Zhong, S. Komarneni, W. Hu, S-vacancy-rich NiFe-S nanosheets based on a fully electrochemical strategy for large-scale and quasi-industrial OER catalysts, Appl. Catal. B-Environ. 345 (2024) 123686.

[55] C. Wang, P. Zhai, M. Xia, W. Liu, J. Gao, L. Sun, J. Hou, Identification of the origin for reconstructed active sites on oxyhydroxide for oxygen evolution reaction, Adv. Funct. Mater. 35 (2023) 2209307.

[56] Y. Pan, X. Xu, Y. Zhong, L. Ge, Y. Chen, J.-P.M. Veder, D. Guan, R. O'Hayre, M. Li, G. Wang, H. Wang, W. Zhou, Z. Shao, Direct evidence of boosted oxygen evolution over perovskite by enhanced lattice oxygen participation, Nat. Commun. 11 (2020) 2002.

[57] X. Xu, Y. Pan, Y. Zhong, C. Shi, D. Guan, L. Ge, Z. Hu, Y.-Y. Chin, H.-J. Lin, C.-T. Chen, H. Wang, S.P. Jiang, Z. Shao, New undisputed evidence and strategy for enhanced lattice-oxygen participation of perovskite electrocatalyst through cation deficiency manipulation, Adv. Sci. 9 (2022) 2200530.

[58] Z.-H. Yin, Y. Huang, K. Song, T.-T. Li, J.-Y. Cui, C. Meng, H. Zhang, J.-J. Wang, Ir single atoms boost metal-oxygen covalency on selenide-derived NiOOH for direct intramolecular oxygen coupling, J. Am. Chem. Soc. 146 (2024) 6846–6855.

[59] Z.-F. Huang, J. Song, S. Dou, X. Li, J. Wang, X. Wang, Strategies to break the scaling relation toward enhanced oxygen electrocatalysis, Matter 1 (2019) 1494–1518.

[60] P. Li, S. Zhao, Y. Huang, Q. Huang, B. Xi, X. An, S. Xiong, Corrosion resistant multilayered electrode comprising Ni$_3$N nanoarray overcoated with NiFe-phytate complex for boosted oxygen evolution in seawater electrolysis, Adv. Energy Mater. 14 (2024) 2303360.

[61] W. Tong, M. Forster, F. Dionigi, S. Dresp, R. Sadeghi Erami, P. Strasser, A.J. Cowan, P. Farras, Electrolysis of low-grade and saline surface water, Nat. Energy 5 (2020) 367–377.

[62] L. Yu, L. Wu, B. McElhenny, S. Song, D. Luo, F. Zhang, Y. Yu, S. Chen, Z. Ren, Ultrafast room-temperature synthesis of porous S-doped Ni/Fe (oxy)hydroxide electrodes for oxygen evolution catalysis in seawater splitting, Energy Environ. Sci. 13 (2020) 3439–3446.